Smart Materials and
Structures

PAPER • **OPEN ACCESS**

Structural and damping performance of hybrid GFRP composites with thin sheet SMA inserts

To cite this article: Dusan Milosavljevic *et al* 2026 *Smart Mater. Struct.* **35** 015030

IOP Publishing Smart Mater. Struct. 35 (2026) 015030 https://doi.org/10.1088/1361-665X/ae3266

Smart Materials and Structures

RECEIVED
17 July 2025

REVISED
28 November 2025

ACCEPTED FOR PUBLICATION
31 December 2025

PUBLISHED
8 January 2026

PAPER

Structural and damping performance of hybrid GFRP composites with thin sheet SMA inserts

Dusan Milosavljevic[*], **Alberto Zecchetto, Nora Lecis and Simone Cinquemani**

Department of Mechanical Engineering, Politecnico di Milano, Via Giuseppe La Masa 1, 20165 Milan, Italy
[*] Author to whom any correspondence should be addressed.

E-mail: dusan.milosavljevic@polimi.it

Keywords: SMA, NiTi, Cu–Al–Mn, GFRP, damping, hybrid composite, interfacial adhesion

Abstract

This work explores a novel hybrid composite design that incorporates thin shape memory alloy (SMA) sheet inserts within glass fiber-reinforced polymer laminates. By using flat NiTi and Cu–Al–Mn alloy plates—instead of traditional SMA wires—the study evaluates whether increased material volume improves vibration damping. Brass inserts were also tested as a non-transforming control. The composites were subjected to free vibration, tensile, and flexural testing. NiTi inserts yielded the best damping and most consistent mechanical behavior. Cu–Al–Mn inserts showed potential as a lower-cost alternative but exhibited greater variability. Laser-cut patterns in NiTi inserts reduced damping slightly but enhanced flexural strength and interfacial adhesion. The findings underline how SMA type and insert design influence the balance between damping efficiency and structural performance.

1. Introduction

Since their discovery in the middle of the 20th century, shape memory alloys (SMAs) have found application in a wide variety of fields, from aerospace to medicine, as both sensing and actuating devices [1]. Additionally, a significant amount of research effort has gone into potential applications of SMAs in the field of vibration suppression. This interest is driven by the fact that in addition to the intrinsic damping which is present in all materials, SMAs have two additional mechanisms of energy dissipation, one passive and one active [2, 3]. The passive damping mechanism is found in SMAs in twinned martensitic state, and is characterized by an increase in internal friction within the alloy which occurs during load application as consequence of the movement of martensitic variant interfaces and twin boundaries [2–6]. The active damping mechanism is a consequence of the temperature-induced phase transformation of the SMA from the martensitic to the austenitic phase (and reverse), during which the alloy experiences a peak in energy dissipation capacity [7–9]. However, the second mechanism is highly dependent on heating and cooling rates during phase transformation [4].

Due to its high and consistent shape memory and damping performance, NiTi remains the most widely researched and industrially adopted SMA. However, its prohibitive cost and manufacturing complexity have motivated researchers to explore numerous alternatives, with Cu-based SMAs showing significant potential [10]. Over the last decades, considerable effort has focused on mitigating their inherent challenges, such as low workability, brittleness, martensitic stabilization, and comparatively lower shape memory performance [10]. Reducing the aluminum content of the alloy to below ∼18 at.% improved cold workability of the alloy by promoting the formation of a more disordered parent phase and stabilizing a 2 M martensitic microstructure [11–13]. Through the control of the relative grain size in the alloy it was possible to significantly improve both shape memory and damping properties of the alloy, by reducing the dimensionality of the constraints between the grains [14–17]. A damping loss factor of $\tan\delta \approx 0.07$, for the pure martensitic phase, has been recorded in Cu–Al–Mn wires with a relative grain size of $d/D \approx 1$, where d and D are the mean grain size and the wire diameter, respectively [7]. Additionally, a recoverable strain of up to 7% has been achieved in sheets with a relative grain size

$d/t \approx 15.4$, where d and t are the mean grain size and SMA sheet thickness, respectively [17]. Further improvements in Cu–Al–Mn performance can be achieved by introducing additional alloying elements [18].

Most of the current research on the SMA hybrid composites has been focused on the use of NiTi wires [19–23]. Embedding of a woven NiTi wire mesh at volume fractions of ∼5% was shown to substantially increase the stiffness and damping of laminated composites [19]. Additionally, martensitic transformation in embedded NiTi wires contributes to increased tensile strength of the composite, especially an higher temperatures [20]. Cyclical loading fatigue tests have shown that glass-fiber-reinforced epoxy composites embedded with NiTi wires can achieve fatigue life more than twice higher than that of the base composite material [22].

Most of the current research on SMA-hybrid composites has focused on the use of NiTi wires [19–26]. Embedding of woven NiTi wire meshes at volume fractions of ∼5% has been shown to substantially increase the stiffness and damping of laminated composites [19], and early studies demonstrated the feasibility and challenges of integrating NiTi wires within polymer laminates, including issues related to alignment and interfacial bonding [25]. More recent work has continued to investigate wire reinforced systems for vibration control and adaptive stiffness applications [26], with Katsiropoulos *et al* reporting damping ratios of $\zeta \approx 0.03 - 0.04$ in aramid/epoxy composites containing prestrained superelastic NiTi wires [24]. In addition, martensitic transformation in embedded NiTi wires contributes to increased tensile strength of the composite, especially at higher temperatures [20], and fatigue studies have shown that glass fiber-reinforced polymer (GFRP) laminates with NiTi wires can achieve more than twice the fatigue life of the base composite [22].

In this study, the authors propose and investigate a new approach to SMA hybrid composite design by embedding thin SMA sheets, rather than the more commonly used wires, within laminated GFRP composites. This configuration allows for a substantially greater volume fraction of active material, potentially improving the passive damping capacity of the composite and enabling more efficient vibration suppression. All damping tests in this work were conducted at room temperature, where both the NiTi and Cu–Al–Mn SMA inserts are fully martensitic. As a result, the measured damping corresponds to the intrinsic passive damping of the martensitic phase rather than transformation-induced hysteresis. While SMA wires have been widely studied in hybrid systems, few works have focused on the use of thin SMA sheets. This study aims to address that gap by evaluating the performance of thin-sheet SMA hybrid laminates across both damping and mechanical criteria.

Building on this context, NiTi and Cu–Al–Mn were selected as the two SMA insert materials for this study, reflecting their respective positions as the established industry standard and a promising, cost-effective alternative. Their inclusion enables an evaluation of how each material performs in the form of thin sheet inserts within GFRP laminates, particularly in terms of damping effectiveness and structural response. This comparative approach is intended to provide insight into their respective advantages and limitations when used in this novel composite configuration.

In addition to this comparative evaluation, the authors also considered the potential challenge posed by embedding continuous SMA plates, which could make the composite more susceptible to delamination at the insert interface. To address this concern, a set of specimens was fabricated using SMA inserts featuring elliptical hole patterns cut by laser. These patterns were intended to promote resin flow and mechanical interlocking between layers, thereby improving adhesion across the insert region and reducing the risk of delamination in the hybrid composite structure.

2. Materials and methods

2.1. Specimen fabrication

For this study, composite materials were fabricated using prepreg layers of a GFRP combined with thin sheets of NiTi and Cu–Al–Mn SMAs. In addition to these two SMA-based systems, the study also includes a third configuration incorporating commercial brass sheets. Brass, like Cu–Al–Mn, is a copper-based alloy, but it lacks the martensitic transformation and associated damping mechanisms characteristic of SMAs. It therefore serves as a valuable baseline reference, allowing the authors to isolate and quantify the functional benefits imparted by the SMA behavior. By comparing brass, Cu–Al–Mn, and NiTi inserts across damping, tensile, and flexural tests, this study provides a comprehensive evaluation of how material selection and interface behavior affect the multifunctional performance of SMA hybrid composites. Details regarding the fabrication of the SMA inserts and the subsequent composite are provided in the sections below.

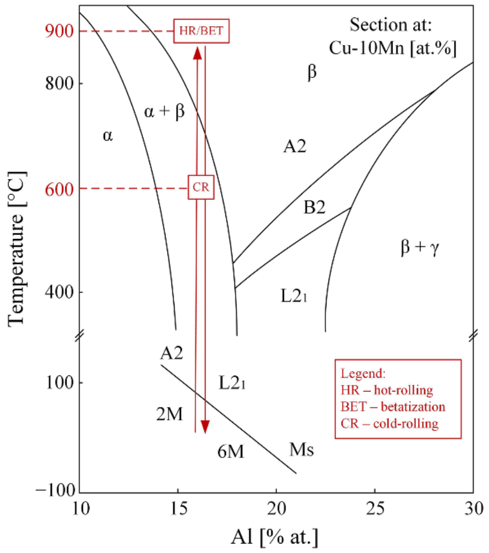

Figure 1. Section of the ternary Cu–Al–Mn phase diagram at 10 at.% of Mn, with the treatment temperatures highlighted.

2.1.1. SMA thin sheet inserts

The Cu–Al–Mn SMA sheet samples were produced from raw materials (copper, aluminum, and manganese) with a minimum purity of 99.98 wt.%. The choice of the Cu-16Al-10Mn at.% composition was motivated by the high material workability of Cu–Al–Mn alloys with low aluminum content (below 18 at.%) [11, 12]. Moreover, at this specific ratio of aluminum and manganese, the alloy exists in the martensitic phase at room temperature [11, 27]. This phase in Cu–Al–Mn alloys is generally characterized by a high passive damping capacity, and a damping capacity greater than in the austenitic phase [7, 16]. A set of Cu–Mn pre-alloys was first cast using a vacuum arc melting furnace. Subsequently, the final alloy was obtained by a second casting in an Ages–Galloni induction melting furnace under a mild argon stream, with the addition of the necessary amounts of copper and aluminum to the pre-alloys. Casting the alloy into a graphite mold yielded a final ingot with a thickness of approximately 10 mm. To obtain a thin sheet of the Cu–Al–Mn SMA alloy, the ingot underwent a rolling treatment consisting of two phases: hot-rolling and cold-rolling. The hot-rolling process involved heating the ingot to 900 °C (within the single β-phase region, shown as HR in figure 1) before passing it through a rolling mill with 30 cm diameter rolls.

This process incrementally reduced the ingot thickness to approximately 2 mm. Further reduction of thickness was achieved by cold-rolling because at such low thicknesses, the combined effect of high temperature and high pressure can cause manganese oxidation, potentially altering the alloy composition and its mechanical and shape memory properties [6]. Cold-rolling achieved a final SMA sheet thickness of approximately 0.4 mm. During the cold-rolling process, a single recovery heat treatment was performed at the halfway point by holding the SMA alloy at 600 °C (within the $\alpha + \beta$ dual-phase region, shown as CR in figure 1) for 10 min. The final heat treatment applied to the Cu–Al–Mn SMA sheets was betatization at 900 °C for 10 min, followed by quenching in cold water to achieve a martensitic structure and activate the shape memory properties of the alloy.

The NiTi SMA sheet samples used in the study were commercially acquired and also had a thickness of 0.4 mm. A differential scanning calorimetry test was performed on samples of both Cu–Al–Mn and NiTi SMA materials to confirm that their phase transformation temperatures would result in the alloys being in the martensitic state at room temperature.

In addition to being affected by alloy composition, the properties of SMA alloys, especially damping performance, are influenced by the relative grain size (d/t), defined as the ratio between the mean grain size (d) in the alloy sample and the sample thickness (t) [16]. In this study, the relative grain size for samples of both SMA alloys was calculated, where the mean grain size (d) was estimated from optical microscopy (Nikon ECLIPSE LV150NL, Nishioi, Shinagawa-ku, Tokyo, Japan) images using the formula $d = 2 \times \sqrt{A/\pi N}$. Here, A represents the area of a circle within which the mean grain size was observed, and N is a measure of the grain density within that area, calculated as $N = N_1 + 0.5N_2$, where N_1 is the number of grains entirely inside the circle and N_2 is the number of grains intersecting the border. The relative grain size was then determined by dividing this mean grain size (d) by the sample thickness (t).

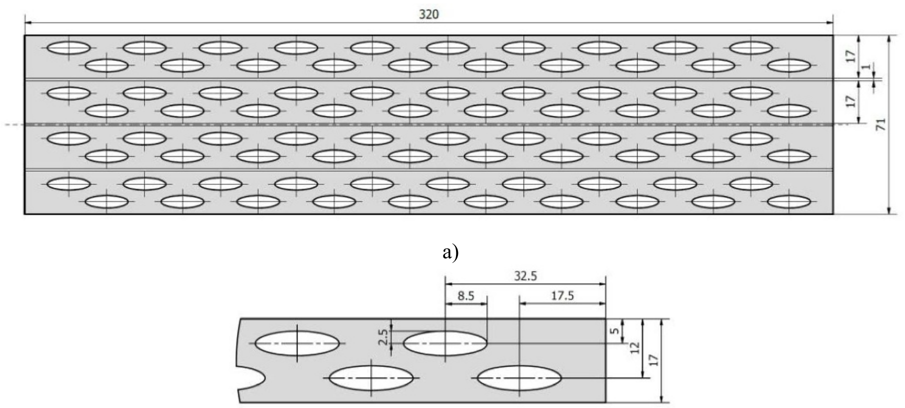

a)

b)

Figure 2. Schematic of the elliptical hole pattern laser-cut into the NiTi SMA sheet (dimensions in millimeters): (a) the full NiTi SMA sheet as received, and the elliptical hole pattern and overall dimensions. Longitudinal lines indicate the planned 1 mm wide cutting paths to section the sheet into four 17 mm wide elongated specimens for subsequent damping tests after composite lamination, (b) a cutout detailing a single insert intended as a layer within the damping composite sample, illustrating the dimensions and positioning of the elliptical holes.

The relative grain sizes of the Cu–Al–Mn and NiTi SMA sheets were determined to be 0.42 and 0.41, respectively, making them directly comparable.

Following the fabrication processes described above, the pristine SMA sheets were ready for embedding in the composite. In addition to the pristine sheets, a set of NiTi sheets underwent a laser cutting operation to create an elliptical hole pattern (see figure 2).

The patterned NiTi sheets were embedded as layers in the composite material in the same way as the pristine NiTi and Cu–Al–Mn thin sheets, with the intention of exploring the trade-off between better attachment of the composite layers through the holes in the NiTi insert and the potential loss of damping due to the reduced amount of NiTi SMA in the composite specimen.

The elliptical shape of the holes, with the major axis oriented longitudinally, was chosen to reduce the notch effect under delaminating loads applied in that direction. The dimensions of the ellipses were selected based on findings reported in a previous study [28], which indicated that smaller openings would not allow sufficient GFRP attachment through the holes. Simultaneously, increasing the removed area further would predictably lead to a more substantial loss of damping performance due to the reduction of the NiTi SMA.

The laser cutting operation was performed using a customized version of the BLM group LC5 laser cutting machine (LC5, Adige-SYS S.p.A. BLM Group, Levico Terme, Italy). The machine was equipped with the YLS-6000-CUT (IPG Photonics Corp., Oxford, Massachusetts) high-power multi-mode fiber laser source and used the Pro cutter 2.0 (HPSSL, Precitec GmbH & Co., Gaggenau, Germany) laser cutting head. Figure 3 shows the aluminum support designed to prevent bending or flapping of the thin NiTi sheet during the laser cutting, which was assisted by nitrogen gas.

2.1.2. Composite lamination

As outlined in the introduction, the composite material was based on pre-impregnated (prepreg) plies of GFRP. These epoxy glass prepreg plies, characterized by a dry weight of 300 g m^{-2} and a resin content of 37%–42%, were produced by Mako Shark (Dolzago, Italy).

To ensure a more predictable and stable response during both damping and mechanical testing, and avoid undesired twisting and warping, the stacking sequence was made both symmetric and balanced. Using a symmetric lamination sequence decouples in-plane loads from bending deformations and applied moments from causing in-plane strains [29]. Thus, in-plane forces result primarily in in-plane deformations, while applied moments primarily cause bending [29].

Employing a balanced lamination sequence further eliminated coupling between normal strains and shear stresses, and vice versa [29]. The selected stacking sequence was [0/insert/0/90/90]s, where 'insert' denotes either the SMA or brass thin sheets (see figure 4). In free vibration tests, especially with SMA inserts that locally increase stiffness, a purely unidirectional laminate would lead to strong anisotropy in bending stiffness and potential coupling between bending and torsion. The inclusion of 90° plies mitigates these effects and ensures a more uniform bending response. Furthermore, this cross-ply architecture

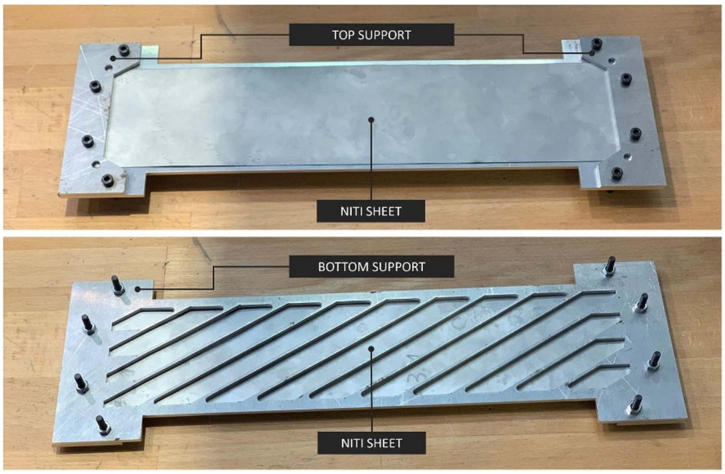

Figure 3. Top and bottom view of the aluminum support with a NiTi SMA sheet mounted on it.

0
insert
0
90
90
90
90
0
insert
0

Figure 4. The [0/insert/0/90/90]s lamination sequence of the GFRP composite. The diagram illustrates the stacking order of the prepreg layers, with the positions of the SMA or brass inserts highlighted in yellow. The symmetry of the layup about the mid-plane is evident.

provides a representative configuration for typical GFRP laminates used in general structural applications, while maintaining a balanced and stable mechanical response around the insert.

During composite lamination, a sufficient number of prepreg layers were placed between the inserts to position them away from the composite centerline. This offset was intentional because material closer to the neutral axis experiences less strain during bending or vibration, thus minimizing the contribution of the insert's damping properties to the overall composite response. By placing the inserts away from the centerline, they undergo greater strain and can more effectively contribute to their damping characteristics. The composite curing was performed at a temperature of 175 °C. Subsequently, individual samples for damping, tensile, and three-point bending tests were obtained from the bulk composite material by cutting using a lubricated microcutting machine equipped with a diamond-coated blade.

2.2. Experimental setup and design

2.2.1. Damping performance estimation

The damping performance of the composite materials was determined by measuring and analyzing the rate of exponential decay in their oscillation response following an induced displacement at the free end [30].

Four types of composite samples were tested in this study, based on the insert material used between the GFRP layers: brass, Cu–Al–Mn, NiTi, and patterned NiTi. Rectangular specimens with a cross-section of 17 × 2.8 mm^2 and a length of 330 mm were cut from the bulk composite material. The inserts themselves were 320 mm long, with an additional 10 mm of pure GFRP at one end to facilitate clamping during the cantilever beam testing setup.

For each test, a cantilever boundary condition was created by clamping one end of the specimen. The samples were excited by introducing a displacement at the free end of the clamped beam. The resulting time-domain displacement of the free end was measured using an M5L/20 laser distance sensor (MEL Mikroelektronik GmbH, Breslauer Str. 2, D-85386 Eching, Germany) with a 20 mm range. Since

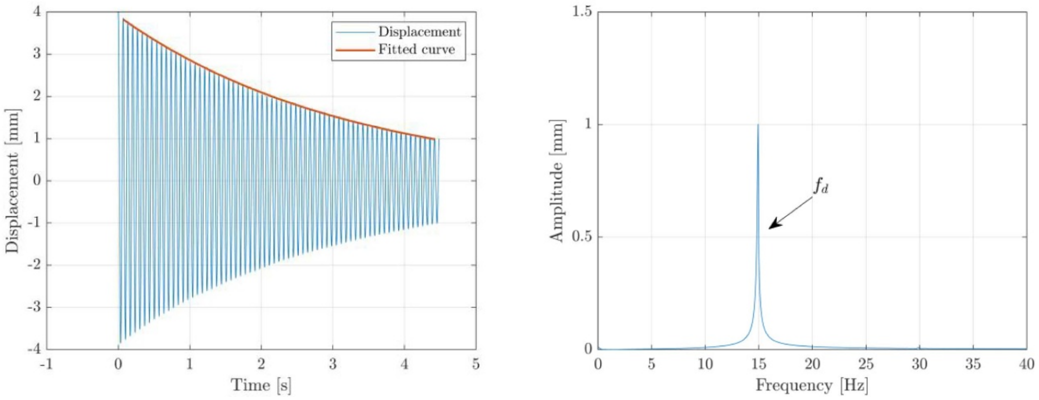

a) b)

Figure 5. (a) Typical time-domain displacement response of a NiTi composite specimen during free vibration (blue line), illustrating the exponential decay. The red line represents the fitted exponential envelope ($y(t) = A_0\mathrm{e}^{-\alpha t}$), which was used to determine the exponential decay constant (α) and subsequently calculate the damping ratio. (b) Corresponding frequency-domain response derived from the measured displacement signal, showing the dominant peak at the damped natural frequency f_d used in the damping calculations.

the response was dominated by the first bending mode, the system was modeled as an equivalent single-degree-of-freedom oscillator for damping identification.

The recorded signal was filtered using a moving median filter to suppress high frequency noise and any minor contribution from higher vibration modes, which effectively isolated the first mode response used for damping estimation (figure 5(b)).

The damping analysis for each measurement was performed on the portion of the response envelope between 4 mm and 1 mm of the signal amplitude.

The dominant vibration frequency f_d for each measurement was determined using the Fast Fourier Transform of the measured displacement signal (figure 5(b)), and the corresponding damped angular frequency was calculated as:

$$\omega_\mathrm{d} = 2\pi f_\mathrm{d} = \omega_\mathrm{n}\sqrt{1-\zeta^2} \tag{1}$$

where ω_n is the undamped natural angular frequency, and ζ is the damping ratio [31, 32]

The exponential decay constant α (s^{-1}), was determined by extracting the peaks of the decaying displacement signal and fitting them using MATLAB's Curve Fitting Toolbox with an exponential model in the form of:

$$y(t) = A_0\mathrm{e}^{-\alpha t} \tag{2}$$

which represents the amplitude envelope of an underdamped system response, described by:

$$x(t) = A_0\mathrm{e}^{-\alpha t}\sin(\omega_\mathrm{d} t + \phi) \tag{3}$$

where $\alpha = \zeta\omega_\mathrm{n}$.

By substituting into equation (1) and solving for ζ, the following relation was obtained and used to compute the damping ratio for each measurement:

$$\zeta = \frac{\alpha}{\sqrt{\alpha^2 + \omega_\mathrm{d}^2}}. \tag{4}$$

2.2.2. Tensile testing

The tensile testing and subsequent data processing of the results was performed according to the guidelines found in the ASTM D3039 standard for testing tensile properties of composite materials with a polymer matrix [33]. This included determining the ultimate tensile strength, the tensile chord modulus of elasticity (in the 0.1%–0.3% strain range), and the failure type for the composites [33]. As in the damping estimation tests, four types of composite specimens were tested, based on the insert material: brass, Cu–Al–Mn, NiTi, and patterned NiTi. Rectangular specimens with a cross-section of 17×2.8 mm^2 and a length of 160 mm were cut from the bulk composite. To ensure failure occurred within the gauge section and prevent slippage in the grips, tabs were bonded to each end of the tensile samples using epoxy glue. These GFRP tabs had a cross-section of 2 × 17 mm and a length of 36 mm, featuring a bevel on the interior edge [33]. The necessity of using tabs arose from the observation that without them, or with every cloth applied directly to the specimen, failure occurred within the gripping section. The strain measurements during testing were performed using an extensometer and a gauge length of 50 mm. The tensile testing was carried out on a calibrated MTS Alliance RT/100 tensile testing machine (MTS Systems GmbH, Hohentwielsteig 3, D-14153 Berlin-Zehlendorf, Germany) under a constant 2 mm min^{-1} strain rate until specimen failure.

2.2.3. Three point bending

Three point bending tests and the analysis of acquired data was performed according to the guidelines found in the ASTM D7264 standard for testing flexural properties of polymer matrix composite materials [34]. The tests were used to determine the maximum flexural stress and strain of the composite materials, as well as their flexural moduli [34]. All four types of composite material were also tested in three point bending. The specimen had a rectangular cross-section with dimensions 17 × 2.8 mm^2 and a length of 60 mm. The testing was performed on MTS Criterion Model 42 electromechanical load frame (MTS Systems GmbH, Hohentwielsteig 3, D-14153 Berlin-Zehlendorf, Germany) using a 50 mm support span and a loading rate of 1 mm min^{-1}.

3. Results and discussion

3.1. Damping performance

The damping performance was evaluated across four composite types based on their insert material: brass, Cu–Al–Mn, NiTi, and patterned NiTi.

The damping ratio for each measurement was determined by fitting an exponential decay function to the oscillation response peaks. The goodness of fit for these models was consistently high, with R-square values all being greater than 0.994.

A typical free-vibration response of a NiTi composite specimen is shown in figure 5, illustrating both the exponential decay of the measured displacement and the corresponding frequency-domain spectrum. The time-domain signal, together with its fitted exponential envelope, was used to identify the decay constant (α), while the frequency spectrum provided the damped natural frequency (f_d) employed in the damping calculations.

Figure 6 shows the normalized displacement envelopes obtained from the free-vibration measurements for each composite configuration. For each specimen, a decaying envelope was plotted based on the mean value of the exponential decay constant (α) determined from multiple measurements, while the shaded regions around the mean envelopes represent the range between the fastest and slowest decays recorded for that specimen. The close overlap of the envelopes and the narrow extent of the shaded regions indicate that the measured responses were highly consistent across repeated tests. This repeatability is further confirmed quantitatively through an ANOVA analysis [35], presented later in section 3.1.

The damping performance of the composite materials is presented in figure 7. Damping ratios are shown as means with error bars representing the standard error of the mean (SEM) from multiple specimens.

Figure 7 reveals that composites with brass inserts exhibit the lowest damping performance. This is anticipated, given the absence of additional microstructural mechanisms for damping enhancement in brass compared to the SMAs. Both Cu–Al–Mn and NiTi SMA inserts, which were in their martensitic phase during the damping tests, demonstrate significantly higher damping performance than the brass composites. Specifically, the Cu–Al–Mn composite showed a 78% increase in damping, while the NiTi composite exhibited a 180% increase compared to the brass composite. This enhanced damping in the martensitic phase of SMAs is attributed to increased internal friction arising from the accommodation of different martensitic variants, movement of twin boundaries, and detwinning [2, 3]. These observed damping ratios for the composites are notably higher than those typically reported for common engineering materials, with flexural damping ratios for aluminum and steel being around 5×10^{-5} and between 1×10^{-4} and 3×10^{-4}, respectively [36].

A direct comparison between the two SMA composites shows that the mean damping ratio of the Cu–Al–Mn based composite is approximately 36% lower than that of the composite with commercial NiTi inserts. While both SMA inserts shared a roughly comparable relative grain size (as described in section 2.1.1), the NiTi composite exhibits superior performance in this state. However, it is noteworthy that previous studies have indicated that both preload application, as well as thermal treatments aimed

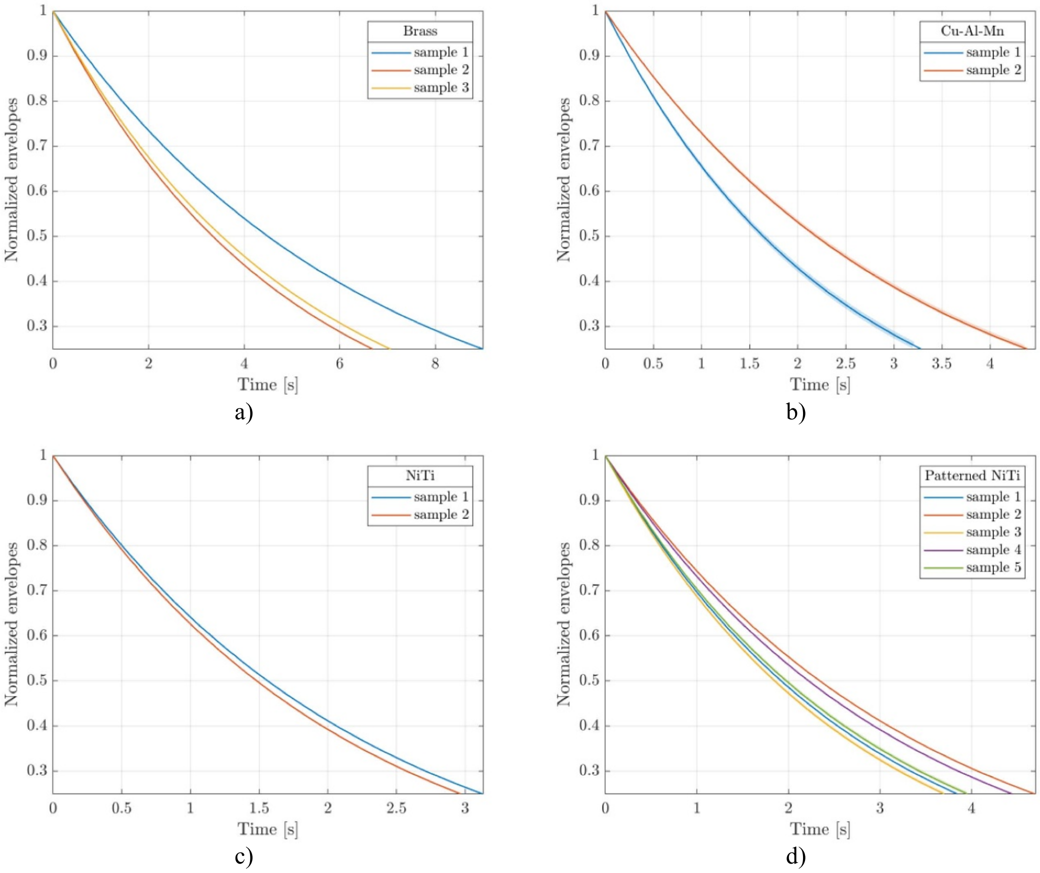

Figure 6. Normalized displacement envelopes of all measurements for each composite configuration: (a) brass, (b) Cu–Al–Mn, (c) NiTi, (d) patterned NiTi. Solid lines represent the mean envelopes identified for each specimen, while the shaded regions denote the range between the fastest and slowest decays measured across repeated tests. The narrow extent of these shaded regions indicates the good repeatability of the experimental measurements.

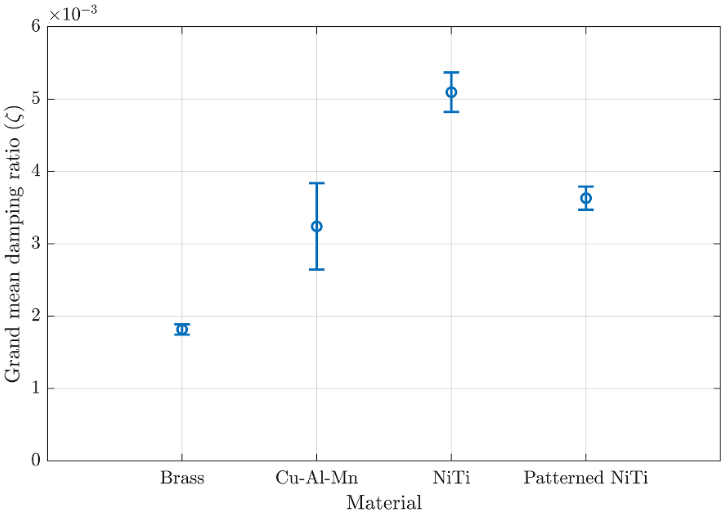

Figure 7. Grand mean damping ratio (ξ) of composite materials with different embedded metallic inserts. Results are shown for brass, Cu–Al–Mn, NiTi, and patterned NiTi inserts. Error bars indicate the standard error of the mean (SEM) calculated from multiple specimens for each material type.

at increasing grain growth in Cu–Al–Mn, can significantly enhance the damping performance of Cu–Al–Mn alloys, potentially making them competitive with NiTi [6, 16].

Lastly, the use of patterned NiTi inserts resulted in a 24.5% reduction in damping ratio compared to pristine NiTi inserts. Although this reduction roughly corresponds to the 28.7% decrease in NiTi

Table 1. Two-way nested ANOVA of damping performance by material and specimen.

Source of variation	Sum of squares	Degrees of freedom	Mean square	*F*-statistic	*P*-value
Material	3.52×10^{-5}	3	1.17×10^{-5}	18.1	<0.001
Specimen (material)	5.20×10^{-6}	8	6.50×10^{-7}	358.6	<0.001
Error	3.63×10^{-8}	20	1.81×10^{-9}		
Total	4.04×10^{-5}	31			

volume, it should not be interpreted as a direct proportionality. This reduction reflects the combined influence of the modified strain distribution and the smaller amount of SMA material. This observation highlights the joint effect of patterning on damping behavior, interfacial adhesion, and material usage by illustrating the trade-off between performance, delamination resistance, and potential cost. Despite this reduction in damping performance, subsequent mechanical testing, as elaborated in section 3.2, demonstrates that patterning significantly improves the composite's resistance to delamination.

To contextualize these damping levels with prior research on SMA-wire composites, Zhang *et al* [19] reported room-temperature logarithmic attenuation coefficients of about 0.10–0.14 for epoxy laminates containing up to 5.35 vol.% of prestrained martensitic NiTi wires, corresponding to damping ratios of roughly $1.6\text{–}2.2 \times 10^{-2}$. In comparison, the present NiTi-sheet composites achieved a mean damping ratio of $\sim 5.1 \times 10^{-3}$ at an SMA volume fraction of ∼28 vol.%, while the Cu–Al–Mn and patterned NiTi variants reached $\sim 3.3 \times 10^{-3}$ and $\sim 3.6 \times 10^{-3}$, respectively (figure 7). Although the absolute values are lower, it should be emphasized that specimens in the Zhang *et al* study were prestrained, which enhances energy dissipation through stress-induced twin-boundary motion. In addition, the laminates in that case were based on CFRP prepregs with a [CC/epoxy/CC] type lay-up, whereas the present study used GFRP prepregs with a [0/insert/0/90/90]s stacking sequence. These differences in fiber reinforcement, stiffness, and laminate design further limit the direct comparability of the absolute damping ratios. The present laminates, by contrast, were tested in the as-fabricated, unstressed martensitic state, showing the intrinsic passive damping that can be obtained from such sheet inserts, as previous studies have shown that stress-induced transformation cycling can lead to low-cycle functional fatigue in NiTi sheets, resulting in energy dissipation capacity loss of 30%–40% [19].

To statistically assess the influence of material type and the specimens on damping performance, a two-way nested ANOVA was performed [35], with the results summarized in table 1.

The ANOVA revealed a statistically significant main effect of material on damping performance ($F(3, 20) = 18.1$, $p < 0.001$), indicating that the average damping ratios differ significantly across the four material types. Furthermore, a highly significant effect of the specimen nested within materials was observed ($F(8, 20) = 358.6$, $p < 0.001$). This significant specimen variability is predominantly driven by differences observed among the Cu–Al–Mn composite specimens. The higher consistency observed in the NiTi-based composites compared to those with Cu–Al–Mn inserts could be primarily attributed to the increased reactivity of Cu–Al–Mn during the thermomechanical treatment phase used to produce thin sheets. This reactivity, especially from the highly reactive Mn component, combined with the sensitivity of Cu–Al–Mn's shape memory and mechanical properties to slight variations in the Al/Mn ratio, likely contributed to the higher variability seen in the Cu–Al–Mn-based composites [6, 10, 37]. Additionally, this variability is further compounded by the fact that the Cu–Al–Mn inserts were fabricated in a laboratory setting, unlike the commercially produced NiTi and brass inserts. Laboratory-scale production inherently introduces greater specimen-to-specimen inconsistency due to subtle fluctuations in processing conditions, cooling rates, or microstructural uniformity that are typically better controlled in commercial manufacturing.

3.2. Mechanical performance

To evaluate the mechanical performance of the different composite configurations, tensile tests were performed on a total of 14 specimens (3 with brass, 5 with Cu–Al–Mn, 3 with NiTi, and 3 with patterned NiTi inserts) following the ASTM D3039 standard. The collected data allowed for the determination of mechanical properties such as the ultimate tensile strength, ultimate tensile strain, and tensile chord modulus of elasticity (0.1%–0.3% strain range), as well as the types of failure. The results, summarized in table 2, and depicted by representative stress–strain curves in figure 8, provide insight into the comparative mechanical behavior of composites with different SMA and brass inserts. For these composite specimens, failure was defined as the point at which any individual constituent layer was compromised. In all composite specimens incorporating SMA-based inserts, a lateral failure within the gauge length

Table 2. Average ultimate tensile strength, ultimate tensile strain, and tensile chord modulus of elasticity (0.1%–0.3% strain range) for brass, Cu–Al–Mn, NiTi, and patterned NiTi composite specimens. Values represent the mean ± standard deviation, and the corresponding coefficient of variation.

Materials	σ_{UTSavg} (MPa)	σ_{UTSstd} (MPa)	σ_{UTScv} (%)	$\varepsilon_{\mathrm{UTSavg}}$ (%)	$\varepsilon_{\mathrm{UTSstd}}$ (%)	$\varepsilon_{\mathrm{UTScv}}$ (%)	Ec_{avg} (MPa)	Ec_{std} (MPa)	Ec_{cv} (%)
Brass	441	32	7	2.2	0.4	18	36.1	2.5	6.9
Cu–Al–Mn	343	64	19	1.8	0.2	11	28.9	1.30	5
NiTi	372	12	3	2.2	0.1	5	22.2	0.3	1.4
NiTi patterned	266	23	9	1.7	0.2	12	19.2	0.8	4.2

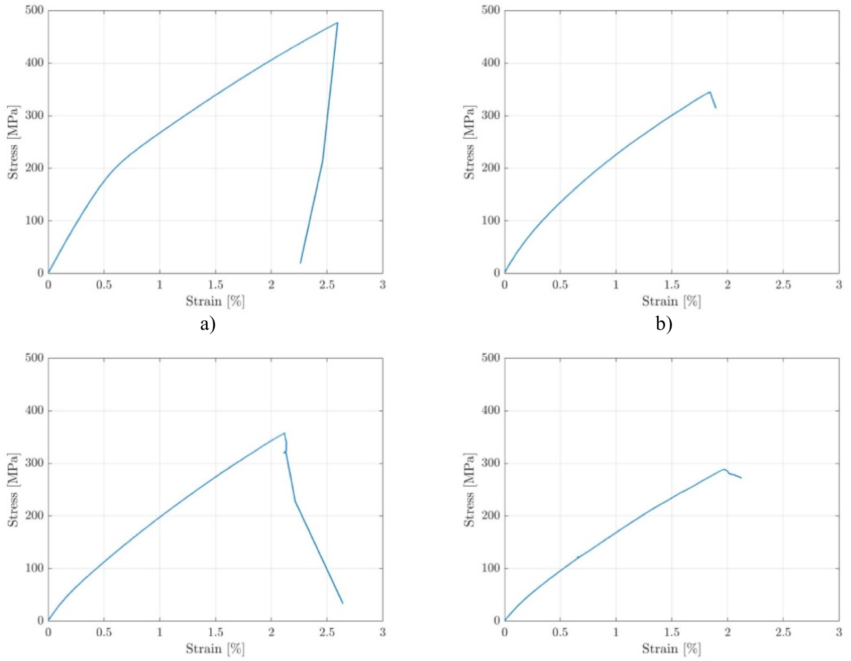

a) b) c) d)

Figure 8. Representative stress–strain responses for each of the four composite materials that were tested: (a) brass, (b) Cu–Al–Mn, (c) NiTi, (d) patterned NiTi.

was observed. This failure occurred exclusively within the GFRP layers (both outer and internal plies), while the SMA inserts remained unbroken. In contrast, for specimens with brass inserts, the failure was also lateral but propagated through the entire thickness of the specimen, affecting both the GFRP plies and the brass insert.

In terms of ultimate tensile strength, the brass-based composite specimens exhibited the highest performance, reaching an average of 441 MPa, indicating the strongest reinforcement effect under tension. Composites incorporating NiTi inserts followed closely, with a UTS of 372 MPa and notably low variability, highlighting their stable and repeatable mechanical behavior. The composites with Cu–Al–Mn inserts achieved a respectable UTS of 343 MPa, but showed high variability, likely due to bonding inconsistencies introduced by slight warping during the quenching process.

The lowest UTS was observed in composites containing patterned NiTi inserts, averaging 266 MPa. This reduction in strength is likely due to the notch effect caused by the patterned holes, which introduce localized stress concentrations. Interestingly, these patterned specimens were the only ones that did not exhibit delamination during tensile testing, a characteristic that remains consistent in the subsequent three-point bending tests, suggesting a potentially beneficial interfacial behavior despite their lower strength.

In terms of strain at ultimate tensile strength ($\varepsilon_{\mathrm{UTS}}$), both the brass and NiTi-based composites exhibited the highest average strain, reaching 2.2%, suggesting that these configurations are capable of accommodating significant deformation before failure. Notably, the NiTi-based composites again demonstrated exceptional consistency, with a coefficient of variation (CoV) of just 5%, reinforcing their mechanical reliability under tensile loading. The bilinear stress–strain response observed in brass-based composites reflects the staged mechanical engagement of the ductile insert, figure 7(a). The initial linear

Table 3. Average maximum flexural strength, maximum flexural strain, and flexural chord modulus of elasticity (0.1%–0.3% strain range) for brass, Cu–Al–Mn, NiTi, and patterned NiTi composite specimens. Values represent the mean ± standard deviation, and the corresponding coefficient of variation.

Materials	σ_{MAXav} (MPa)	σ_{MAXstd} (MPa)	σ_{MAXcv} (MPa)	$\varepsilon_{\mathrm{MAXavg}}$ (%)	$\varepsilon_{\mathrm{MAXstd}}$ (%)	$\varepsilon_{\mathrm{MAXcv}}$ (%)	E_{avg} (GPa)	E_{std} (GPa)	E_{cv} (MPa)
Brass	654	11	2	2.7	0.1	4	40	0	0
Cu–Al–Mn	316	100	32	1.7	0.6	35	25	6	24
NiTi	142	116	82	1.5	1.4	93	12	2	17
Patterned NiTi	365	69	19	2.1	0.3	14	27	2	7

region is governed by the elastic behavior of the GFRP layers, while the subsequent slope reduction indicates yielding of the brass, which continues to carry load and contributes to the laminate's overall toughness. This behavior accounts for both the high ultimate tensile strength and the observed variability in strain to failure.

In contrast, the Cu–Al–Mn specimens showed a slightly lower average strain of 1.8%, accompanied by a moderate CoV of 11%, indicating more variability in the deformation behavior. The lowest $\varepsilon_{\mathrm{UTS}}$ was recorded in the patterned NiTi composites, averaging 1.7%, with a CoV of 12%. This reduced strain capacity may be attributed to early stress concentrations around the pattern edges, which can initiate localized damage and restrict elongation. Despite this limitation, the patterned specimens maintained structural integrity by avoiding delamination.

A slight non-linearity observed at low strain levels in several specimens may originate from process-induced residual stresses, generated during the curing process due to the thermal expansion mismatch between the inserts and the GFRP. Similar 'toe-in' behavior has been reported in unidirectional composite specimens due to fiber alignment and micro-slip effects under initial tensile loading [38–40].

Regarding stiffness, as represented by the tensile chord modulus, the brass-based composites exhibited the highest average value at 36.1 GPa. This elevated modulus is consistent with the significant elastic contribution of the ductile brass insert. However, this group also displayed the highest variability in stiffness, which may suggest variations in the uniform engagement of the brass insert under initial loading.

The Cu–Al–Mn composites showed a moderate average modulus of 28.9 GPa with improved uniformity, indicating a more consistent load-sharing mechanism between the insert and surrounding plies. NiTi-based composites, while possessing a lower average modulus of 22.2 GPa, were notably consistent, reflecting a highly repeatable elastic response. In contrast, the patterned NiTi composites exhibited the lowest average stiffness of 19.2 GPa and moderate variability. This reduced stiffness is likely attributed to the local compliance introduced by the hole patterns, which effectively decrease the load-bearing cross-section of the hybrid structure.

Three point bending tests were performed on a total of 20 specimens (5 per each composite type) following the ASTM D7264 standard.

Through these tests it was possible to determine the flexural properties of the composites such as the maximum flexural stress, maximum flexural strain, and flexural chord modulus of elasticity (0.1%–0.3% strain range). The summary of the results is given in table 3. Failure under three-point bending was defined as the point at which the specimen either exhibited delamination between the insert and the surrounding GFRP plies, or fractured.

The three-point bending results revealed clear distinctions in flexural performance among the tested hybrid composites. Brass-based specimens achieved the highest flexural strength, averaging 654 MPa with negligible variability.

This performance was accompanied by the highest strain at maximum flexural stress of 2.7% and flexural chord modulus of 40 GPa. The patterned NiTi specimens showed a significantly improved average strength of 365 MPa, more than doubling that of the pristine NiTi configuration. While they showed slightly higher variability, their mechanical response remained relatively stable, with a high stiffness of 27 GPa and no signs of delamination.

In contrast, the pristine NiTi and Cu–Al–Mn specimens exhibited substantial performance deficits, both in terms of average strength and repeatability. NiTi in particular showed low flexural strength and high variability, along with a low modulus and premature failure. Both it and the Cu–Al–Mn group consistently experienced delamination at the insert-GFRP interface, a failure mechanism not observed in the brass or patterned NiTi specimens. This strongly suggests that interfacial stability is a decisive factor in flexural performance. The patterned inserts likely promote better mechanical interlocking, while brass benefits from inherent ductility and compatibility with the surrounding matrix. Together, these results underline the importance of insert design and bonding quality in determining the structural effectiveness of hybrid composite laminates under flexural loading.

4. Conclusion

This study presents a novel approach to SMA-hybrid composite design by replacing traditional SMA wires with thin sheet SMA inserts, aiming to maximize active material volume for enhanced vibration damping performance. Through comparative analysis of NiTi, Cu–Al–Mn, and brass inserts in GFRP laminates, the work evaluates both the damping and structural behavior of these new hybrid systems across multiple loading scenarios.

The results demonstrate that NiTi-based composites offer the best overall balance between damping capability and mechanical consistency, particularly in tensile and flexural loading. Their high damping performance, driven by martensitic mechanisms, combined with low variability in strength and stiffness, confirms their suitability for multifunctional applications. Cu–Al–Mn, while less consistent, showed promising damping behavior and moderate mechanical properties, suggesting that with further processing refinement, especially thermal treatments, it may serve as a cost-effective alternative to NiTi. Brass-based composites, though lacking in damping performance, exhibited the highest tensile and flexural strength and stiffness, making them ideal as a reference material for structural benchmarks.

Importantly, the use of patterned NiTi inserts introduced an effective compromise between damping and mechanical resilience. Although patterning reduced the insert volume and, consequently, damping effectiveness, it significantly improved delamination resistance, leading to better flexural strength and structural reliability compared to unpatterned NiTi. Across both tensile and bending tests, interfacial integrity emerged as a key determinant of performance, with delamination consistently limiting strength and repeatability in specimens with unpatterned NiTi and Cu–Al–Mn inserts.

Overall, this work provides the first systematic evaluation of SMA hybrid composites using thin sheet inserts and highlights the potential of both material selection and insert design to tailor damping and structural performance. These findings lay the groundwork for future research into optimized SMA geometries, surface treatments, and smart structural applications where energy dissipation and load-bearing capacity must be carefully balanced.

Data availability statement

All data that support the findings of this study are included within the article (and any supplementary files).

Acknowledgment

This work was supported by the Office of Naval Research under Grant N00014-20-1-2608.

ORCID iD

Dusan Milosavljevic 0000-0003-2100-0379

References

[1] Kumar P K and Lagoudas D C 2008 SMAs as active materials—applications *Shape Memory Alloys* (Springer) pp 29–40
[2] Van Humbeeck J and Liu Y 2000 The high damping capacity of shape memory alloys *Shape Memory Implants* ed L Yahia (Springer) pp 46–60
[3] Van Humbeeck J 2003 Damping capacity of thermoelastic martensite in shape memory alloys *J. Alloys Compd.* **355** 58–64
[4] San Juan J and Nó M L 2003 Damping behavior during martensitic transformation in shape memory alloys *J. Alloys Compd.* **355** 65–71
[5] Elmay W, Peltier L, Gabrion X, Kubler R, Piotrowski B, Laheurte P and Berveiller S 2022 Damping capacity of Ti–Nb shape memory alloys evaluated through DMA and single-impact tests *Shap. Mem. Superelasticity* **8** 349–55
[6] Milosavljevic D, Bassani P, Cinquemani S and Lecis N 2023 Effects of thermomechanical treatments on Cu–Al–Mn shape memory alloys *Mater. Chem. Phys.* **302** 127756
[7] Koeda N, Omori T, Sutou Y, Suzuki H, Wakita M, Kainuma R and Ishida K 2005 Damping properties of ductile Cu-Al-Mn-based shape memory alloys *Mater. Trans.* **46** 118–22
[8] Chang S-H, Chien C and Wu S-K 2016 Damping characteristics of the inherent and intrinsic internal friction of $Ti_{50}Ni_{50-x}Fe_x$ ($x = 2$, 3, and 4) shape memory alloys *Mater. Trans.* **57** 351–6
[9] Wu S-K, Chan W-J and Chang S-H 2017 Damping characteristics of inherent and intrinsic internal friction of Cu-Zn-Al shape memory alloys *Metals* **7** 397
[10] Alaneme K K and Okotete E A 2016 Reconciling viability and cost-effective shape memory alloy options—a review of copper and iron based shape memory metallic systems *Eng. Sci. Technol. Int. J.* **19** 1582–92

[11] Kainuma R, Takahashi S and Ishida K 1995 Ductile shape memory alloys of the Cu-Al-Mn system *J. Phys. IV* **05** C8–961–C8–966
[12] Sutou Y, Omori T, Kainuma R and Ishida K 2008 Ductile Cu-Al-Mn based shape memory alloys: general properties and applications *Mater. Sci. Technol.* **24** 896–901
[13] Mallik U S and Sampath V 2008 Effect of composition and ageing on damping characteristics of Cu-Al-Mn shape memory alloys *Mater. Sci. Eng.* **478** 48–55
[14] Sutou Y, Omori T, Wang J J, Kainuma R and Ishida K 2004 Characteristics of Cu-Al-Mn-based shape memory alloys and their applications *Mater. Sci. Eng.* **378** 278–82
[15] Sutou Y, Omori T, Yamauchi K, Ono N, Kainuma R and Ishida K 2005 Effect of grain size and texture on pseudoelasticity in Cu-Al-Mn-based shape memory wire *Acta Mater.* **53** 4121–33
[16] Sutou Y, Omori T, Koeda N, Kainuma R and Ishida K 2006 Effects of grain size and texture on damping properties of Cu-Al-Mn-based shape memory alloys *Mater. Sci. Eng.* **438–440** 743–6
[17] Sutou Y, Omori T, Kainuma R and Ishida K 2013 Grain size dependence of pseudoelasticity in polycrystalline Cu-Al-Mn-based shape memory sheets *Acta Mater.* **61** 3842–50
[18] Sutou Y, Kainuma R and Ishida K 1999 Effect of alloying elements on the shape memory properties of ductile Cu–Al–Mn alloys *Mater. Sci. Eng.* **273–275** 375–9
[19] Zhang R, Ni Q-Q, Masuda A, Yamamura T and Iwamoto M 2006 Vibration characteristics of laminated composite plates with embedded shape memory alloys *Compos. Struct.* **74** 389–98
[20] Payandeh Y, Meraghni F, Patoor E and Eberhardt A 2012 Study of the martensitic transformation in NiTi–epoxy smart composite and its effect on the overall behavior *Mater. Des.* **39** 104–10
[21] Daghash S M and Ozbulut O E 2016 Characterization of superelastic shape memory alloy fiber-reinforced polymer composites under tensile cyclic loading *Mater. Des.* **111** 504–12
[22] Wang Z, Xu L, Sun X, Shi M and Liu J 2017 Fatigue behavior of glass-fiber-reinforced epoxy composites embedded with shape memory alloy wires *Compos. Struct.* **178** 311–9
[23] Mirzaei A H, Shokrieh M M and Saeedi A 2022 Fatigue behavior of laminated composites with embedded SMA wires *Compos. Struct.* **293** 115753
[24] Katsiropoulos C V, Pappas P, Koutroumanis N, Kokkinos A and Galiotis C 2020 Improving the damping behavior of fiber-reinforced polymer composites with embedded superelastic shape memory alloys (SMA) *Smart Mater. Struct.* **29** 025006
[25] Lau K 2002 Vibration characteristics of SMA composite beams with different boundary conditions *Mater. Des.* **23** 741–9
[26] Patil R A, Rane S B and Kumbhar S B 2021 Investigation on dynamic behaviour of shape memory alloy (SMA) wire embedded composite *IOP Conf. Ser.: Mater. Sci. Eng.* **1136** 012024
[27] Milosavljevic D, Lecis N and Cinquemani S 2024 Influence of thermomechanical treatments and chemical composition on the phase transformation of Cu-Al-Mn shape memory alloy thin sheets *Appl. Sci.* **14** 10406
[28] Milosavljevic D, Lecis N and Cinquemani S 2023 Experimental assessment to evaluate adhesion in hybrid composite structures containing shape memory alloy layers *Proc. SPIE* **12483** 85–93
[29] Barbero E J 2017 Common laminate types *Introduction to Composite Materials Design, Third Edition* (CRC Press) pp 187–96
[30] Casiano M J 2016 *Extracting Damping Ratio from Dynamic Data and Numerical Solutions* (Marshall Space Flight Center, NASA)
[31] Meirovitch L 2010 Response of single-degree-of-freedom systems to initial excitations *Fundamentals of Vibrations* (Waveland Press) pp 80–93
[32] Cai L W 2016 Vibrations of single-DOF systems *Fundamentals of Mechanical Vibrations* (ASME-Wiley) pp 81–185
[33] D30 Committee Test method for tensile properties of polymer matrix composite materials
[34] D30 Committee Test method for flexural properties of polymer matrix composite materials
[35] Miller R G Analysis of variance (ANOVA) *Beyond Anova: Basics of Applied Statistics Chapman & Hall Texts in Statistical Science Series* (Chapman & Hall/CRC) pp 119–29
[36] Cremer L and Heckl M 1988 *Structure-Borne Sound* (Springer)
[37] Kumar P K and Lagoudas D C 2008 Introduction to shape memory alloys *Shape Memory Alloys* (Springer) pp 1–51
[38] Daniel I M, Ishai O, Daniel I M and Daniel I 1994 *Engineering Mechanics of Composite Materials* vol 3 (Oxford university press New York)
[39] Li C, Zobeiry N, Keil K, Chatterjee S and Poursartip A 2014 Advances in the characterization of residual stress in composite structures *Int. SAMPE Technical Conf.*
[40] Seers B, Tomlinson R and Fairclough P 2021 Residual stress in fiber reinforced thermosetting composites: a review of measurement techniques *Polym. Compos.* **42** 1631–47